


Cite this: *Nanoscale Adv.*, 2021, 3, 4702

# Mechanisms of sodiation in anatase TiO<sub>2</sub> in terms of equilibrium thermodynamics and kinetics†

Zhongqiu Tong,<sup>abc</sup> Tianxing Kang,<sup>bc</sup> Jianming Wu,<sup>a</sup> Rui Yang,<sup>bc</sup> Yan Wu,<sup>bc</sup> Ruqian Lian,<sup>\*d</sup> Hui Wang,<sup>bc</sup> Yongbing Tang<sup>de</sup> and Chun Sing Lee<sup>de\*bc</sup>

Anatase TiO<sub>2</sub> is a promising anode material for sodium-ion batteries (SIBs). However, its sodium storage mechanisms in terms of crystal structure transformation during sodiation/de-sodiation processes are far from clear. Here, by analyzing the redox thermodynamics and kinetics under near-equilibrium states, we observe, for the first time, that upon Na-ion uptake, the anatase TiO<sub>2</sub> undergoes a phase transition and then an irreversible crystal structure disintegration. Additionally, unlike previous theoretical studies which investigate only the two end points of the sodiation process (*i.e.*, TiO<sub>2</sub> and NaTiO<sub>2</sub>), we study the progressive crystal structure changes of anatase TiO<sub>2</sub> upon step-by-step Na-ion uptake (Na<sub>x</sub>TiO<sub>2</sub>, *x* = 0.0625, 0.125, 0.25, 0.5, 0.75, and 1) for the first time. It is found that the anatase TiO<sub>2</sub> goes through a thermodynamically unstable intermediate phase (Na<sub>0.25</sub>TiO<sub>2</sub>) before reaching crystalline NaTiO<sub>2</sub>, confirming the inevitable crystal structure disintegration during sodiation. These combined experimental and theoretical studies provide new insights into the sodium storage mechanisms of TiO<sub>2</sub> and are expected to provide useful information for further improving the performance of TiO<sub>2</sub>-based anodes for SIB applications.

Received 17th May 2021  
Accepted 24th June 2021

DOI: 10.1039/d1na00359c

rsc.li/nanoscale-advances

## 1. Introduction

Current research in titanium dioxide (TiO<sub>2</sub>) has made promising advances towards applications in photocatalysis,<sup>1</sup> dye-sensitized solar cells,<sup>2</sup> capacitors,<sup>3</sup> and rechargeable batteries such as lithium-ion batteries (LIBs) and sodium-ion batteries (SIBs).<sup>4–6</sup> Notably, TiO<sub>2</sub> anode materials of SIBs show superiorities of high theoretical capacity (~336 mA h g<sup>−1</sup> corresponding to NaTiO<sub>2</sub>), moderate redox potential (from 0.5 to 1 V vs. Na<sup>+/</sup>Na), earth abundance, and low cost.<sup>7–9</sup> Among various TiO<sub>2</sub> polymorphs, anatase TiO<sub>2</sub> (a-TiO<sub>2</sub>) possesses two-dimensional diffusion channels along the *a* and the *b* axes with a size of 3.72 × 3.78 Å, which are theoretically suitable for interstitial accommodation of Na-ions (1.02 Å).<sup>10,11</sup> Plenty of a-TiO<sub>2</sub> anode materials for SIBs have been synthesized which delivered high

specific capacities, high-rate performance and long cycling stabilities.<sup>5,9,12–14</sup>

However, the reaction mechanisms on which this remarkable performance is based are still not fully understood. The key issue is to determine the a-TiO<sub>2</sub> crystal structure transformation during the sodiation/de-sodiation processes. In practice, three different mechanisms have been proposed: (1) reversible insertion/extraction of Na-ions in the crystalline lattice,<sup>15–18</sup> (2) Na-ion storage occurring in intermediates of sodium titanium oxide phases produced from a-TiO<sub>2</sub> during initial discharge/charge cycles,<sup>19,20</sup> and (3) a multiphase complex (mainly formed by metallic Ti<sup>0</sup>, low-crystallinity sodium titanates and Ti<sub>x</sub>O<sub>y</sub> with poor crystallinity) derived from a completely collapsed a-TiO<sub>2</sub> structure after the first sodiation/de-sodiation.<sup>14,21–23</sup> All the three proposed Na-ion redox mechanisms find their own support from different experimental results.<sup>23–40</sup> Recently, it was found that the sodiation processes in the internal region and near the surface region of a-TiO<sub>2</sub> particles differed significantly.<sup>35,37,38,41</sup> Furthermore, the literature also demonstrates that the sodiated phase compositions of a-TiO<sub>2</sub> depend strongly on the morphology,<sup>33,42</sup> crystallinity,<sup>43,44</sup> surface status,<sup>24,45–47</sup> particle size,<sup>48</sup> cycling numbers,<sup>23,25,31,47,49</sup> and solid electrolyte interphase (SEI)-controlled Na-ion diffusion kinetics.<sup>23,31,50</sup> These phenomena clearly indicate that the sodiation kinetics occurring in the a-TiO<sub>2</sub> are rather sluggish. The different mechanisms possibly stem from the fact that their corresponding supporting experiments have been carried out under different non-equilibrium sodiation/de-sodiation

<sup>a</sup>College of Materials and Metallurgical Engineering, Guizhou Institute of Technology, Guiyang, 550003, Guizhou, China

<sup>b</sup>Department of Chemistry, City University of Hong Kong, Hong Kong, China. E-mail: apcslee@cityu.edu.hk

<sup>c</sup>Center of Super-Diamond and Advanced Films (COSDAF), City University of Hong Kong, Hong Kong, China

<sup>d</sup>School of Physical Science and Technology, Hebei University, Baoding, 071002, China. E-mail: rqlian@126.com

<sup>e</sup>Shenzhen Institutes of Advanced Technology, Chinese Academy of Sciences, Shenzhen, 518055, China

† Electronic supplementary information (ESI) available. See DOI: 10.1039/d1na00359c



conditions. That is they are likely to be all correct but under different kinetics conditions. Unfortunately, this situation is difficult for researchers to establish the fundamental understanding of the thermodynamics of the sodiation process in a-TiO<sub>2</sub>. In fact, experimental investigations under near-equilibrium conditions have been shown to be useful for understanding the sodiation mechanisms in electrode materials such as NaFePO<sub>4</sub> and hard carbons.<sup>51–55</sup> However, until now, there have been no corresponding studies on the a-TiO<sub>2</sub> anode for elucidating its sodiation mechanism.

In this work, we aim to fill this gap by combining experimental studies such as galvanostatic intermittent titration technique (GITT) and cyclic voltammetry (CV), and density functional theory (DFT) calculation to understand sodiation/desodiation in a-TiO<sub>2</sub>, for the first time. In addition, unlike previous theoretical studies which focus mainly on investigating the properties of the two end points (TiO<sub>2</sub> and NaTiO<sub>2</sub>),<sup>22,43,46,53</sup> we theoretically studied the crystal structure changes of anatase- and amorphous-derived Na<sub>x</sub>TiO<sub>2</sub> under step-by-step Na-ion uptake conditions ( $x = 0.0625, 0.125, 0.25, 0.5, 0.75$ , and  $1$ ). By further supplementation with *ex situ* X-ray photoelectron spectroscopy (XPS) and transmission electron microscopy (TEM), we provide convincing evidence that defect-free a-TiO<sub>2</sub> suffers crystal structure disintegration before reaching the final crystalline NaTiO<sub>2</sub>. Our results also demonstrate that the sodiation process is strongly influenced by the crystallinity of a-TiO<sub>2</sub>, applied discharge/charge current densities and potential windows.

## 2. Experimental

### 2.1 Preparation of TiO<sub>2</sub> samples

TiO<sub>2</sub> samples were prepared by standard hydrolysis and annealing using tetrabutyl titanate.<sup>5,9</sup> Amorphous, low-crystalline and high-crystalline TiO<sub>2</sub> materials (denoted as “amor-TiO<sub>2</sub>”, “low crys-TiO<sub>2</sub>” and “high crys-TiO<sub>2</sub>”, respectively) were prepared by annealing treatments of the hydrolysis-obtained precipitate in air at 310 °C for 1 h, 450 °C for 0.5 h and 500 °C for 10 h, respectively.

### 2.2 Physical characterization

A thermogravimetry analysis/differential scanning calorimetry (TGA/DSC) system (Netzsch, STA 449C) was used to determine the suitable annealing temperature of the hydrolysis-obtained precipitate in air. The crystalline and morphology information was collected by X-ray diffraction (XRD, PANalytical X'Pert Pro X-ray diffractometer), transmission electron microscopy (TEM, FEI Tecnai G2F30, 300 kV), high-resolution TEM (HRTEM), selected area electron diffraction (SAED), and scanning electron microscopy (SEM, FEI Helios Nanolab 600i) examinations. X-ray photoelectron spectroscopy tests (XPS, PHI 5700ESCA System) and Raman spectra (JY Co. LABRAM-HR) were used to study chemical elements and bond characters. Nitrogen physisorption measurements were performed on a Quantachrome QDS-MP-30 analyzer (USA) at 77 K.

### 2.3 Electrochemical measurements

For the electrochemical measurements, TiO<sub>2</sub> slurry (80 wt% titania, 10 wt% conductive carbon and 10 wt% PVDF (poly(vinylidene fluoride))) was pasted on a copper substrate and dried in a vacuum. The mass loading of the active material was about 2 mg cm<sup>−2</sup>. Na-ion half-cells were assembled into 2032 type coin cells with a sodium foil counter electrode, a Whatman glass fiber separator, and 1 M NaClO<sub>4</sub>/ethylene carbonate-propylene carbonate (EC-PC, volume ratio of 1 : 1) electrolyte. Li-ion half-cells were assembled into 2032 type coin cells with a lithium foil counter electrode, a Whatman glass fiber separator, and 1 M LiClO<sub>4</sub>/ethylene carbonate-propylene carbonate (EC-PC, volume ratio of 1 : 1) electrolyte. Galvanostatic discharge/charge and galvanostatic intermittent titration technique (GITT) tests were conducted using an Arbin Instrument system. All the tests were conducted at room temperature.

### 2.4 DFT calculations

Calculations employing the density functional theory (DFT) + *U* method were implemented in the Vienna *Ab initio* Simulation Package (VASP), where *U* is the on-site Coulomb parameter.<sup>22</sup> Valence electrons in these calculations were described using a plane-wave basis set with an energy cutoff of 500 eV. Interactions between core and valence electrons were described with the PAW method, with cores of [Mg] for Ti, [He] for O, and [Ne] for Na. Lattice systems were modeled with periodic boundary conditions. Full relaxation of all atomic positions was carried out until the forces on all atoms were less than 0.5 eV nm<sup>−1</sup> for geometric and energetic convergence.

## 3. Results and discussion

### 3.1 Physical characterization and electrochemical performance

Because of the respectively controlled annealing treatments at temperatures of 310, 450 and 500 °C (Fig. S1a†), the amorphous, the low-crystallinity and the high-crystallinity TiO<sub>2</sub> samples (denoted as “amor-TiO<sub>2</sub>”, “low crys-TiO<sub>2</sub>” and “high crys-TiO<sub>2</sub>”, respectively) exhibit nearly identical morphologies (Fig. 1a–c), almost the same specific surface areas (Fig. S1b†) but different degrees of crystallinity (Fig. 1d and S1c–f†). The crystalline structure of anatase TiO<sub>2</sub> with two-dimensional diffusion channels is demonstrated in Fig. 1e. The random Ti and O atom arrangements of amorphous TiO<sub>2</sub> are presented in Fig. 1f.

The sodiation/desodiation performances of the three titania electrodes were studied at various current densities over the potential range of 0.01–2.5 V vs. Na/Na<sup>+</sup>. The discharge/charge profiles and the corresponding differential (dQ/dV) curves during the initial five cycles at 50 mA g<sup>−1</sup> are shown in Fig. 2a–f. The Na-ion storage performances of a super P electrode (mixture of super P and PVDF) and pure high crys-TiO<sub>2</sub> (mixture of high crys-TiO<sub>2</sub> and PVDF) electrodes as well as the Li-ion storage performance of the amor-TiO<sub>2</sub> electrode at 50 mA g<sup>−1</sup> were also tested for comparison (Fig. S2a to f†). Based on the electrochemical properties, three points are notable.



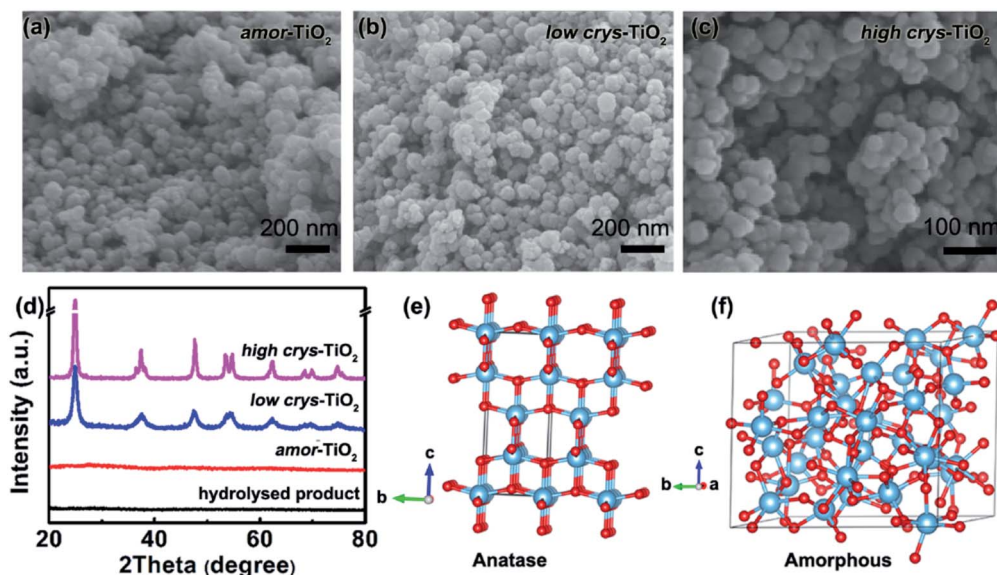


Fig. 1 SEM images of the amorphous-TiO<sub>2</sub> (a), the low crystalline-TiO<sub>2</sub> (b) and the high crystalline-TiO<sub>2</sub> (c) nanoparticles. (d) XRD patterns of the three types of titania nanoparticles. Structural models of the anatase (e) and the amorphous (f) TiO<sub>2</sub>.

(1) Compared to the three titania electrodes (Fig. 2a–f), the super P (Fig. S2a, b†) and the pure high crystalline-TiO<sub>2</sub> (Fig. S2c, d†) electrodes demonstrate different discharge/charge profiles and low discharge/charge capacity, indicating that the super P component only acts as an efficient electron pathway to assist the efficient sodiation/de-sodiation in the active titania.

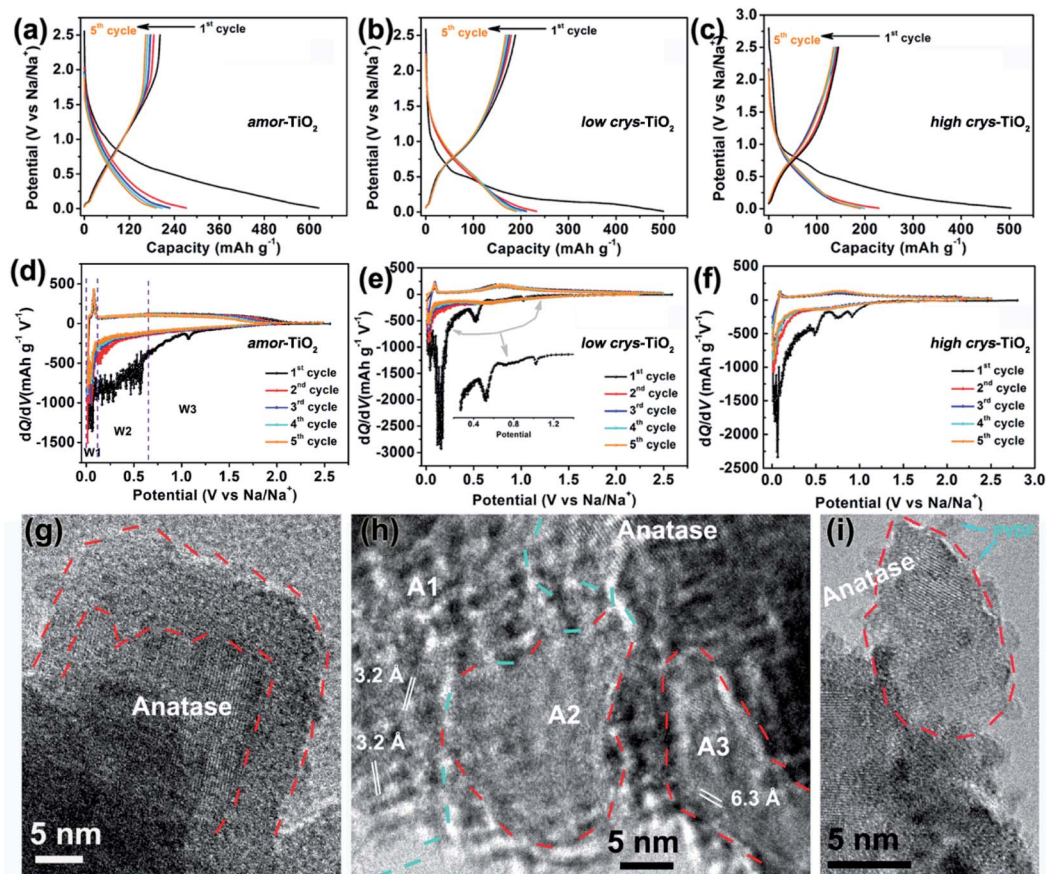


Fig. 2 Discharge/charge profiles of the amorphous-TiO<sub>2</sub> (a), the low crystalline-TiO<sub>2</sub> (b) and the high crystalline-TiO<sub>2</sub> (c) electrodes at 50 mA g<sup>-1</sup>, respectively. Differential (dQ/dV) curves of the discharge/charge profiles of the amorphous-TiO<sub>2</sub> (d), the low crystalline-TiO<sub>2</sub> (e) and the high crystalline-TiO<sub>2</sub> (f) electrodes at 50 mA g<sup>-1</sup>, respectively. (g)–(i) Typical HRTEM images taken from the high crystalline-TiO<sub>2</sub> after the initial full sodiation at 50 mA g<sup>-1</sup>.





(2) Basically, in the 1<sup>st</sup> discharge process of the amor-TiO<sub>2</sub> electrode (Fig. 2d), the differential (dQ/dV) curve of the 1<sup>st</sup> sodiation process can be roughly divided into three potential parts, W1 (0.01 to 0.11 V), W2 (0.11 to 0.65 V) and W3 (0.65 to 2.5 V). (i) In the W1 region, by comparing with the electrochemical features of the super P electrode over the same potential region (Fig. S2b†),<sup>55,56</sup> plating of metallic sodium in the pores of the electrode film makes a large energy storage contribution. (ii) A large difference appeared in the W2 region. It is found that the 1<sup>st</sup> sodiation behavior of the amor-TiO<sub>2</sub> electrode (Fig. 2d) is similar to that of its 1<sup>st</sup> lithiation process (Fig. S2f†) with mild metal-ion insertion-derived structure transformation and relaxation.<sup>8,9</sup> In contrast, for the two crystalline titania samples (low crys-TiO<sub>2</sub> and high crys-TiO<sub>2</sub>, Fig. 2e, f), their high dQ/dV values in the W2 region indicate that they undergo significant structure transformation during 1<sup>st</sup> Na-ion insertion. Furthermore, compared to that for the high crys-TiO<sub>2</sub> electrode (Fig. 2f), a strong peak located at 0.14 V for the low crys-TiO<sub>2</sub> electrode (Fig. 2e) indicates its sodiation feasibility because of low crystallinity.<sup>43,44</sup> (iii) The dQ/dV peaks in the W3 region (Fig. 2d–f) can be assigned to the side reactions, including decomposition of electrolytes and formation of a solid-electrolyte interphase (SEI).<sup>57,58</sup> (iv) The dQ/dV profiles of 1<sup>st</sup> de-sodiation and the following sodiation/de-sodiation cycles (2<sup>nd</sup> to 5<sup>th</sup> cycles) in the three titania electrodes are similar to each other as well as to those of the amor-TiO<sub>2</sub> Li-ion electrode. This phenomenon indicates that the sodiated products might be of amorphous or low-crystallinity nature.<sup>8,9,59</sup>

(3) The amor-TiO<sub>2</sub> electrode delivers better rate capability than the low crys-TiO<sub>2</sub> and the high crys-TiO<sub>2</sub> electrodes (Fig. S2g†). Capacities of 94.7, 80.2 and 72.1 mA h g<sup>−1</sup> are observed at 1.5 A g<sup>−1</sup> for the amor-TiO<sub>2</sub>, the low crys-TiO<sub>2</sub> and the high crys-TiO<sub>2</sub> electrodes, respectively. Additionally, the three titania electrodes demonstrate impressive cycling stability at 500 mA g<sup>−1</sup> for 1000 cycles (Fig. S2h†).

The three titania electrodes under typical potentials of 0.65 and 0.01 V during the initial sodiation process were collected for further XPS analysis. The observation of only Ti<sup>4+</sup> in the three titania electrodes confirms that no redox occurs above 0.65 V (Fig. S3a–c†). Additionally, the co-existence of Ti<sup>4+</sup> and Ti<sup>3+</sup> signals at 0.01 V indicates that the Na-ion storage is from the Ti<sup>4+</sup>/Ti<sup>3+</sup> redox couple under 50 mA g<sup>−1</sup> (Fig. S3d–f†). Meanwhile the different molar ratios of Ti<sup>4+</sup>:Ti<sup>3+</sup> of the three titania electrodes indicate their crystallinity-dependent redox activity.

HRTEM analysis was used for studying the phases of high crys-TiO<sub>2</sub> after the 1<sup>st</sup> full sodiation under 50 mA g<sup>−1</sup>. It is found that sodiation does not change the particle morphology of the sample (Fig. S4a†). Furthermore, as shown in the SAED pattern (Fig. S4b†), diffraction rings from unreacted a-TiO<sub>2</sub>, irregular diffraction points and amorphous diffraction signals confirm that the sodiated product is a mixture of these. As shown in Fig. 2g, the near-surface part of an a-TiO<sub>2</sub> particle suffers Na-ion insertion-derived amorphization, generating a crystalline/amorphous core/shell structure. Fig. 2h demonstrates another typical sodiated titania microsite with complex phases. Besides the homogeneous contrast amorphous area (“A2”), two inhomogeneous contrast amorphous parts (“A1” and “A3”) are also

found, which are believed to be generated from the non-equilibrium sodiation process.<sup>8,9,59,60</sup> Interestingly, some ultra-small nanocrystals can be observed in the amorphous matrix. These nanocrystals could be assigned as Na<sub>2</sub>Ti<sub>6</sub>O<sub>13</sub> (*d*<sub>20-1</sub> = 0.63 Å, JCPDS no. 14-0277) and Na<sub>4</sub>TiO<sub>4</sub> (*d*<sub>041</sub> = 0.32 Å, JCPDS no. 25-1297). As shown in Fig. 2i demonstrating a nanoparticle marked with a dashed line, a large part of anatase TiO<sub>2</sub> has been transformed into a product with low crystallinity, instead of amorphous sodium titanate. Additionally, an unreacted a-TiO<sub>2</sub> nanoparticle is also observed (Fig. S4c†).

Based on the above analysis on the sodiation/de-sodiation performance and XPS results, the crystallinity-dependent sodiation confirms the sluggish redox kinetics in a-TiO<sub>2</sub>. Meanwhile, the complex sodiation products indicate the non-uniform and non-equilibrium sodiation in the a-TiO<sub>2</sub> electrode under such conventional galvanostatic discharge/charge processes at 50 mA g<sup>−1</sup>.<sup>58,61</sup> Thus, investigation of the Na-ion sodiation/de-sodiation in aspects of equilibrium thermodynamics and kinetics could be key to understanding the sodiation/de-sodiation redox mechanism of a-TiO<sub>2</sub>.<sup>51,52,54</sup>

### 3.2 GITT thermodynamic and kinetic analysis

The galvanostatic intermittent titration technique (GITT), as a technique combining transient and steady-state measurements, is widely employed for studying redox thermodynamics and kinetics in systems at near-equilibrium states.<sup>51,52,54,62,63</sup> During the GITT measurements, the three titania electrodes undergo discharge/charge at 25 mA g<sup>−1</sup> for 1 h, followed by a 24 h relaxation process at room temperature (Fig. 3, S5†). GITT measurements of Na-ion redox of the super P (Fig. S6†) and Li-ion redox of the amor-TiO<sub>2</sub> electrode (Fig. S7†) were also conducted for comparison. The open-circuit-voltage (OCV) at the end of relaxation is considered to be the thermodynamic equilibrium potential. The discharge (or charge) overpotential is defined as the absolute value of the difference between the OCV and the experimentally measured potential in the discharge (or charge) process.

First, as shown in the 1<sup>st</sup> GITT sodiation (Fig. 3a) and the 1<sup>st</sup> GITT lithiation (Fig. S7a†) of the amor-TiO<sub>2</sub> electrodes, the steadily decreased OCV is assigned to the redox nature of the amorphous hosts.<sup>38,51,52,54,62–65</sup> Additionally, during the 1<sup>st</sup> GITT discharge process, the overpotential (voltage differences between the blue lines and the valley tips of the black lines in Fig. 3a–c) and reaction resistance (Fig. 3g) increase in the sequence of amor-TiO<sub>2</sub>, low crys-TiO<sub>2</sub> and high crys-TiO<sub>2</sub> electrodes. These phenomena demonstrate that high crystallinity leads to a high reaction barrier. Furthermore, for the low crys-TiO<sub>2</sub> and the high crys-TiO<sub>2</sub> electrodes, the irregular OCV (Fig. 3b, c) and reaction resistance (Fig. 3g) profiles comprise relatively flat and sloping parts. Such curve profiles indicate that sodiation in a-TiO<sub>2</sub> might involve a phase transition reaction and crystalline structure conversion or disintegration.<sup>54,62,65</sup> Notably, the 1<sup>st</sup> de-sodiation of the low crys-TiO<sub>2</sub> (Fig. 3b) and the high crys-TiO<sub>2</sub> (Fig. 3c) electrodes demonstrates similar GITT charge profiles to Na-/Li-ion GITT charge characteristics of the amor-TiO<sub>2</sub> electrode (Fig. 3a, S7a†). This phenomenon



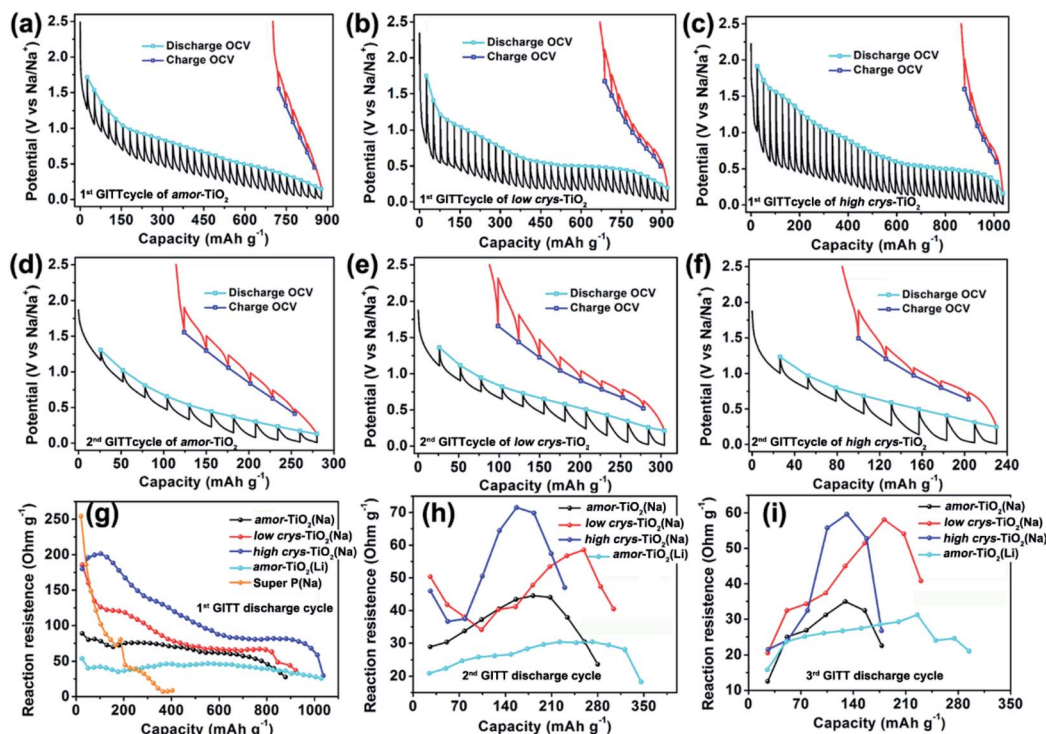


Fig. 3 1<sup>st</sup> GITT sodium-ion uptake/release profiles of the amor-TiO<sub>2</sub> (a), the low crys-TiO<sub>2</sub> (b) and the high crys-TiO<sub>2</sub> (c) electrodes. The hollow square symbols indicate OCVs. 2<sup>nd</sup> GITT sodium-ion uptake/release profiles of the amor-TiO<sub>2</sub> (d), the low crys-TiO<sub>2</sub> (e) and the high crys-TiO<sub>2</sub> (f) electrodes. Plots of discharge reaction resistance vs. capacity for the amor-TiO<sub>2</sub>, the low crys-TiO<sub>2</sub> and the high crys-TiO<sub>2</sub> Na-ion electrodes, and the amor-TiO<sub>2</sub> Li-ion electrode during the 1<sup>st</sup> (g), 2<sup>nd</sup> (h) and 3<sup>rd</sup> (i) GITT discharge cycles.

indicates that the pristine a-TiO<sub>2</sub> crystal structure cannot be recovered after 1<sup>st</sup> near-equilibrium GITT sodiation.<sup>54,62,65</sup>

To better study the near-equilibrium sodiation mechanisms, XPS measurements on Ti valence of the three titania electrodes at 1<sup>st</sup> GITT fully sodiated states were conducted. Ti signals in valences of 0, +2, +3, and +4 (Fig. S8†) are detected for the three titania electrodes. In contrast, as shown in Fig. S3d-f,† Ti signals in valences of only +3 and +4 are observed for the fully discharged titania electrodes treated by the conventional galvanostatic discharge process. The appearance of Ti<sup>0</sup> and Ti<sup>2+</sup> after GITT sodiation confirms the thermodynamic favorability of crystalline structure conversion or disintegration. This result is consistent with the previously reported sodiation/de-sodiation phenomena. It was reported that the phases of sodiated products are applied-current-dependent.<sup>31,35,39</sup> There were differences in the sodiation kinetics occurring in the internal and surface/near-surface regions of a-TiO<sub>2</sub> materials.<sup>35,37,38,41</sup> These two phenomena appear upon non-equilibrium sodiation.

TEM measurements were also conducted to study the near-equilibrium sodiation. Fig. S9† shows typical TEM images of high crys-TiO<sub>2</sub> taken after 1<sup>st</sup> full GITT sodiation. It can be observed that near-equilibrium GITT sodiation also does not change the particle morphology (Fig. S9a, b†). By comparing with the SAED pattern taken from the high crys-TiO<sub>2</sub> electrode treated by the conventional galvanostatic discharge process (Fig. S4b†), it is found that near-equilibrium GITT discharge increases the sodiation-derived amorphization degree

(Fig. S9c†). A typical HRTEM image (Fig. S9d†) shows that the sample consists mostly of the amorphous product and a small amount of low-crystallinity products (marked with blue arrow points). Additionally, the low-crystallinity SAED pattern of high crys-TiO<sub>2</sub> (Fig. S9e,f†) after 1<sup>st</sup> GITT de-sodiation indicates that the sodiation-derived crystal structure disintegration is irreversible. In addition, as to the 2<sup>nd</sup> and 3<sup>rd</sup> GITT sodiation/de-sodiation cycles, the low crys-TiO<sub>2</sub> and the high crys-TiO<sub>2</sub> electrodes demonstrate similar OCV (Fig. 3e, f and S5a-c†) and reaction resistance (Fig. 3h,i) profiles to the amor-TiO<sub>2</sub> as Na-ion (Fig. 3d, S5a†) and Li-ion (Fig. S7b, c†) electrodes. This confirms that the amorphous and low-crystallinity compounds produced during 1<sup>st</sup> GITT sodiation/de-sodiation act as Na-ion hosts during the following cycles.

Second, analysis of ion diffusion coefficients during the GITT sodiation/de-sodiation processes provides information about the Na-ion redox kinetics.<sup>51,52</sup> The Na-ion diffusion coefficient ( $D_{\text{Na}}$ ) and Li-ion diffusion coefficient ( $D_{\text{Li}}$ ) are calculated based on Fick's second law using the equation:<sup>54,62,63</sup>

$$D = \frac{4}{\pi\tau} \left( \frac{m_B V_M}{M_B A} \right)^2 \left( \frac{\Delta E_S}{\Delta E_\tau} \right)^2 \quad (1)$$

where  $\tau$  is the pulse duration,  $m_B$  and  $M_B$  are the active mass and molar mass of the electrochemical material,  $V_M$  is the molar volume,  $A$  is the active surface area of the electrodes,  $\Delta E_S$  is the total change in cell voltage during the current flux, and  $\Delta E_\tau$  is steady-state voltage over the galvanostatic titration. Fig. 4a-c



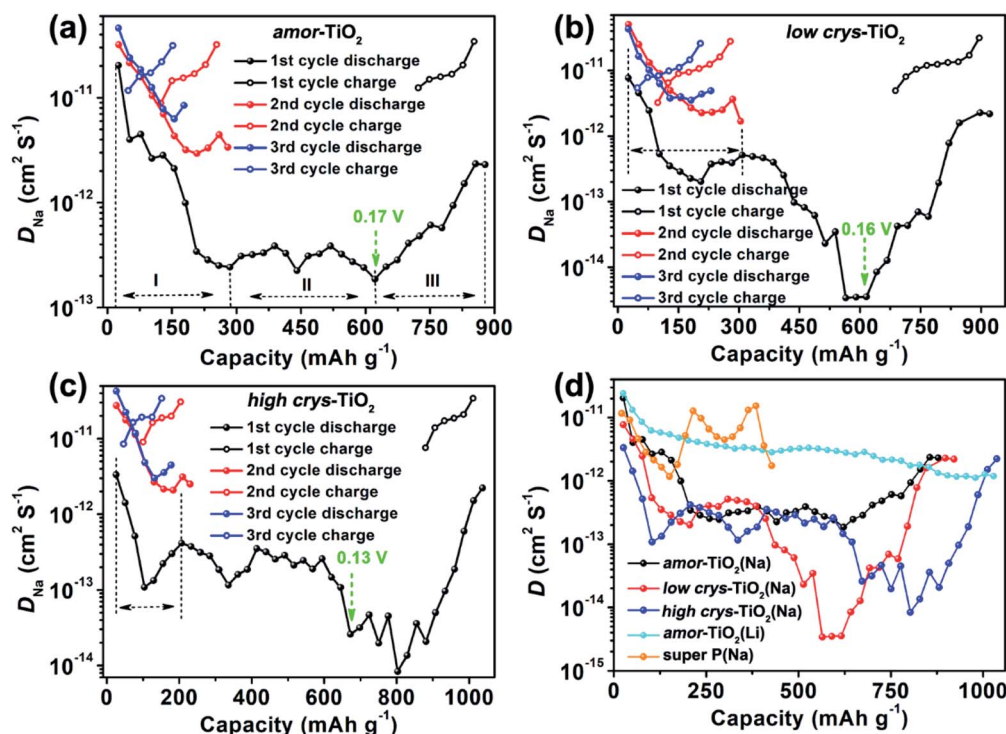


Fig. 4  $D_{\text{Na}}$  determined from the GITT discharge/charge profiles of the amor-TiO<sub>2</sub> (a), the low crys-TiO<sub>2</sub> (b) and the high crys-TiO<sub>2</sub> (c) electrodes of the GITT cycles. (d) Comparison of the  $D$  determined from the 1<sup>st</sup> GITT discharge profiles of the amor-TiO<sub>2</sub>(Na), low crys-TiO<sub>2</sub>(Na), high crys-TiO<sub>2</sub>(Na), and amor-TiO<sub>2</sub>(Li) electrodes.

and S7d† demonstrate  $D_{\text{Na}}$  in the amor-TiO<sub>2</sub>,  $D_{\text{Na}}$  in the low crys-TiO<sub>2</sub>,  $D_{\text{Na}}$  in the high crys-TiO<sub>2</sub>, and  $D_{\text{Li}}$  in the amor-TiO<sub>2</sub> electrodes, respectively.  $D_{\text{Li}}$  values of the 1<sup>st</sup> and the 2<sup>nd</sup> GITT discharge processes in the amor-TiO<sub>2</sub>, low crys-TiO<sub>2</sub> and high crys-TiO<sub>2</sub> over potential ranges of 1 to 3 V were also illustrated (Fig. S10†). The  $D_{\text{Na}}$  profiles of 1<sup>st</sup> GITT sodiation processes in the three titania electrodes and the  $D_{\text{Li}}$  profile of the 1<sup>st</sup> GITT lithiation process in amor-TiO<sub>2</sub> are plotted in Fig. 4d for comparison.

Compared to the steady decrease of  $D_{\text{Li}}$  during the 1<sup>st</sup> GITT lithiation (Fig. 4d and S7d†), the 1<sup>st</sup> GITT sodiation in the amor-TiO<sub>2</sub> electrode shows three distinct stages (marked as I, II and III in Fig. 4a). Before 285 mA h g<sup>-1</sup> (ca. 0.48 V, stage I in Fig. 4a), the continuous  $D_{\text{Na}}$  decrease indicates slow atomic deformation in amorphous titania to accommodate the inserted Na-ions.<sup>38,51,52,54,62–65</sup> Then, the relatively stable  $D_{\text{Na}}$  region from 0.57 to 0.17 V (i.e. from 207.2 to 622 mA h g<sup>-1</sup>, stage II in Fig. 4a) indicates that further sodiation undergoes a redox mechanism similar to that occurring in solid solution hosts.<sup>66–68</sup> Finally, the increase of  $D_{\text{Na}}$  from 0.17 to 0.01 V (stage III in Fig. 4a) can be assigned to the increased electrical conductivity due to the generation of metallic Ti<sup>0</sup> and the plating of metallic sodium.<sup>55,56</sup>

On the other hand, a-TiO<sub>2</sub> undergoes different sodiation kinetics before reaching NaTiO<sub>2</sub> which corresponds to 336 mA h g<sup>-1</sup> (Fig. 4b, c). They show U-shaped  $D_{\text{Na}}$  profiles (marked with dashed lines in Fig. 4b, c) during the 1<sup>st</sup> GITT sodiation. Typically, as demonstrated by the plots of  $D_{\text{Li}}$  vs.

capacity of a-TiO<sub>2</sub> (Fig. S10†), the U-shaped plots of diffusion coefficient vs. capacity (Fig. S10†) indicate the phase transition reaction process.<sup>69–71</sup> In two a-TiO<sub>2</sub> electrodes, the observation of U-shaped  $D_{\text{Na}}$  profiles before reaching the capacity of 336 mA h g<sup>-1</sup> clearly indicates that they undergo a limited phase transition during the 1<sup>st</sup> sodiation processes (marked with dashed lines in Fig. 4b, c). Additionally, the GITT capacity from phase transition occurring in the low crys-TiO<sub>2</sub> reaches 308 mA h g<sup>-1</sup> (corresponding to 0.26 V, Fig. 4b), which is much higher than that of low crys-TiO<sub>2</sub> (206 mA h g<sup>-1</sup>, corresponding to 0.44 V, Fig. 4c). This phenomenon clearly indicates that sodiation in a-TiO<sub>2</sub> is sluggish and crystallinity-dependent.

Following the irreversible phase transition process of the 1<sup>st</sup> GITT sodiation process, the complex changes of  $D_{\text{Na}}$  (Fig. 4d) clearly indicate that the a-TiO<sub>2</sub> undergoes a crystal structure disintegration after the irreversible phase transition.<sup>51,52,54,62,63</sup> The increase of  $D_{\text{Na}}$  from below 0.2 V can be assigned to the increased electrical conductivity because of the generation of metallic Ti<sup>0</sup> and the plating of metallic sodium.<sup>55,56</sup> Notably, this is the first experimental demonstration that the a-TiO<sub>2</sub> crystal structure transformation sequentially contains irreversible phase transition and crystal structure disintegration during initial sodiation under near-equilibrium processes.

### 3.3 Kinetic analysis based on cut-off potential-dependent sodiation/de-sodiation

The above analysis demonstrates that the crystal structure disintegration during 1<sup>st</sup> sodiation is key to influencing the





redox performance of a-TiO<sub>2</sub>. Thus, it is believed that the sodiation/de-sodiation kinetics could be significantly influenced by discharge cut-off potentials. Fig. 5a–c, respectively, show rate performance of the amor-TiO<sub>2</sub>, the low crys-TiO<sub>2</sub> and the high crys-TiO<sub>2</sub> electrodes with different discharge cut-off potentials (0.01, 0.1, 0.2 and 0.4 V vs. Na/Na<sup>+</sup>). The discharge/charge profiles of the titania electrodes at 50 mA g<sup>−1</sup> are shown in Fig. S11.† The amor-TiO<sub>2</sub> electrodes, due to the facile and uniform redox kinetics below the potential of 0.48 V (Fig. 4a), exhibit an almost incremental increase of capacity along with the cut-off potential varying from 0.4 to 0.01 V (Fig. 5a). For the low crys-TiO<sub>2</sub> electrode, because of the maximum crystal structure disintegration-derived dQ/dV values located at ca. 0.14 V (Fig. 2e), the rate capability varies significantly between cut-off potentials of 0.1 and 0.2 V (Fig. 5b). Additionally, the cut-off potential of 0.4 V neighbors the lower potential of the phase transition under near-equilibrium conditions (0.44 V, Fig. 4d). Thus, the poor rate performance of the low crys-TiO<sub>2</sub> electrode over the potential range of 0.4 to 2.5 V can be derived from the lack of crystal structure disintegration (Fig. 5b). In the case of high crys-TiO<sub>2</sub> electrodes, their increased sodiation barrier makes the influence of cut-off potential on capacity more obvious (Fig. 5c), compared to the low crys-TiO<sub>2</sub> electrodes.

Analysis of pseudocapacitance with different cut-off discharge potentials is also employed to study the sodiation/de-sodiation kinetics. For a specific CV scanning rate (*v*), the measured current (*i*) at a fixed potential (*V*) can be quantitatively

separated into capacitive (*k*<sub>1</sub>*v*) and diffusion controlled (*k*<sub>2</sub>*v*<sup>1/2</sup>) responses according to the equation:<sup>72,73</sup>

$$i(V) = k_1v + k_2v^{1/2} \quad (2)$$

Fig. S12–S14†, respectively, demonstrate the CV curves at different scan rates with variable cut-off potentials for the amor-TiO<sub>2</sub>, the low crys-TiO<sub>2</sub> and the high crys-TiO<sub>2</sub> electrodes. The separated CV curves with a cut-off potential of 0.01 V at 0.2 mV s<sup>−1</sup> of the three titania electrodes are demonstrated in Fig. 5d–f, respectively. The plots of capacitive contribution ratio versus scan rate with variable cut-off potentials for the amor-TiO<sub>2</sub>, the low crys-TiO<sub>2</sub> and the high crys-TiO<sub>2</sub> electrodes are presented for comparison in Fig. 5g–i, respectively. The amorphous titania demonstrates feasible structural relaxation below 0.4 V, leading to almost the same capacitive contribution ratio at a specific scan rate under different potential ranges (Fig. 5g). On the other hand, when the cut-off potentials are set as 0.01 and 0.1 V (Fig. 5h), the high and similar capacitive contribution ratios of the low crys-TiO<sub>2</sub> electrodes are due to that these electrodes undergo sufficient crystal structure disintegration below 0.14 V. Additionally, the decrease of the cut-off potential from 0.4 to 0.1 V gradually increases the degree of crystal structure disintegration, leading to the almost incremental changes of capacitive contribution ratios for the low crys-TiO<sub>2</sub> electrodes (Fig. 5h). Finally, the high crys-TiO<sub>2</sub> electrodes demonstrate similar cut-off potential-dependent changes of capacitive contribution ratios to the low crys-TiO<sub>2</sub> electrodes (Fig. 5i). This phenomenon further confirms that the crystal structure

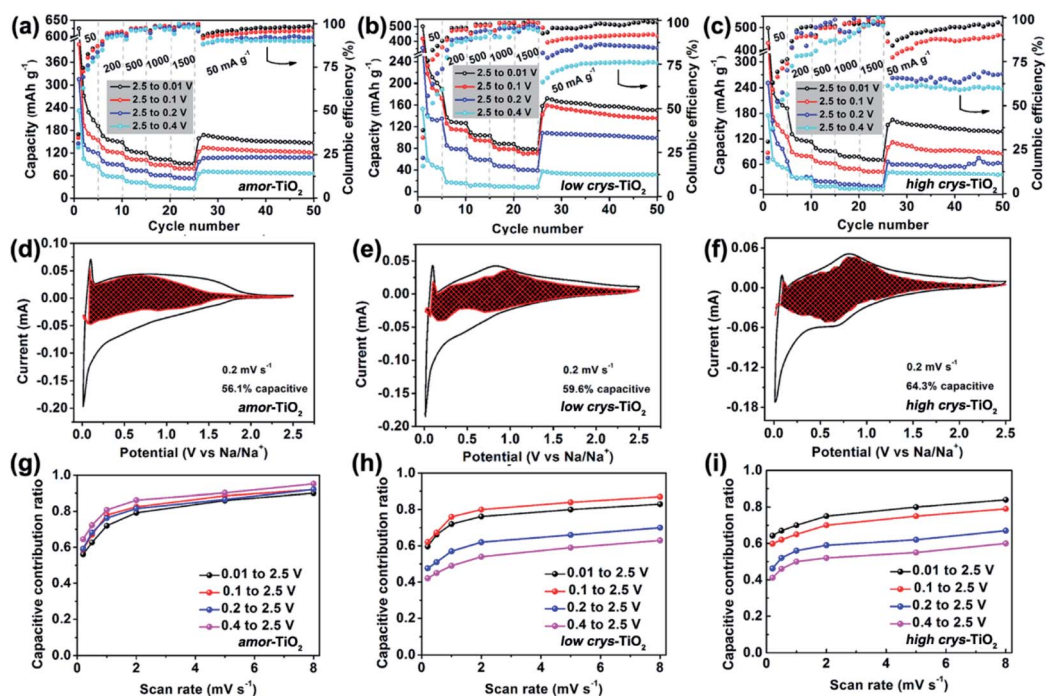


Fig. 5 Rate performance of the amor-TiO<sub>2</sub> (a), the low crys-TiO<sub>2</sub> (b) and the high crys-TiO<sub>2</sub> (c) electrodes over different discharge/charge windows. (b) CV curves of the amor-TiO<sub>2</sub> (d), the low crys-TiO<sub>2</sub> (e) and the high crys-TiO<sub>2</sub> (f) electrodes with separation between total current and surface capacitive current (shaded regions) at 0.2 mV s<sup>−1</sup>. Plots of capacitive contribution ratio versus scan rate under different potential ranges of the amor-TiO<sub>2</sub> (g), the low crys-TiO<sub>2</sub> (h) and the high crys-TiO<sub>2</sub> (i) electrodes.



disintegration-derived amorphous and low-crystalline products are the main Na-ion storage hosts. Notably, in the case of a cut-off potential of 0.1 V, the low crys-TiO<sub>2</sub> electrodes demonstrate higher capacitive contribution ratio than the high crys-TiO<sub>2</sub> electrodes, further indicating the crystallinity-dependent sodiation/de-sodiation kinetics.

When the a-TiO<sub>2</sub> materials are employed as Li-ion hosts in the potential range from 1 to 3 V (Fig. S15†),<sup>11</sup> the low crys-TiO<sub>2</sub> electrode demonstrates higher capacitive contribution ratio than the high crys-TiO<sub>2</sub> electrodes. This result is consistent with the lower crystallinity of the former sample, given that a-TiO<sub>2</sub> is a type of extrinsic pseudocapacitive Li-ion host.<sup>59</sup>

Electrochemical impedance spectroscopy (EIS) was also used to investigate the influence of Na-ion insertion-derived crystal structure disintegration on the redox reversibility. The Nyquist plots of the amor-TiO<sub>2</sub>, the low crys-TiO<sub>2</sub> and the high crys-TiO<sub>2</sub> electrodes after different discharge/charge cycles at 50 mA g<sup>−1</sup> over the potential window of 0.01 to 2.5 V are illustrated in Fig. S16a–c,† respectively. Although the three electrodes demonstrate different charge-transfer resistances (*R*<sub>ct</sub>, which corresponds to the diameter of the semicircle) at the initial assembled state, the low crys-TiO<sub>2</sub> and the high crys-TiO<sub>2</sub> electrodes undergo almost the same changes of *R*<sub>ct</sub> as amor-TiO<sub>2</sub> along with the increase of cycle numbers. This phenomenon indicates that the active materials which act as Na-ion hosts are similar after the activation of the initial discharge/charge process. The amorphous and low-crystallinity compounds produced after the initial discharge/charge cycle are the “true” hosts for Na-ion insertion/extraction during the following cycles.

Based on the above analysis, it is concluded that efficient crystal structure disintegration in a-TiO<sub>2</sub> is key to obtaining high Na-ion storage. To further demonstrate this point, the rate performances of the three titania electrodes were studied with an initial current density of 15 mA g<sup>−1</sup> (Fig. S17†). For both a-TiO<sub>2</sub> electrodes, the increased capacity over the potential range from 0.4 to 0.01 V indicates the increased degree of crystal structure disintegration at 15 mA g<sup>−1</sup> (Fig. S17b, c†), compared to those operating at 50 mA g<sup>−1</sup> (Fig. 2b, c). Due to the reasonably increased degree of crystal structure disintegration in the low crys-TiO<sub>2</sub> electrode, it demonstrates impressive rate performances with 157 and 119 mA h g<sup>−1</sup> at 500 and 1500 mA g<sup>−1</sup> (Fig. S17d†). In contrast, the low crys-TiO<sub>2</sub> electrode only shows 109 and 80.2 mA h g<sup>−1</sup> at 500 and 1500 mA g<sup>−1</sup> when the initial current density is 50 mA g<sup>−1</sup> (Fig. S2g†).

### 3.4 Density functional theory (DFT) calculations on sodiation in the a-TiO<sub>2</sub>

The above electrochemical studies demonstrate the importance of crystal structure disintegration for the a-TiO<sub>2</sub> SIB anodes. This brings a question of why the crystal lattice of a-TiO<sub>2</sub> cannot accommodate the Na-ions for facile insertion/removal, although the size of two-dimensional diffusion channels (a size of 3.72 × 3.78 Å) is much larger than the radius of Na-ions (1.02 Å).<sup>10,11</sup> To answer this question, DFT calculations on the corresponding amorphous and anatase TiO<sub>2</sub>-derived Na<sub>*x*</sub>TiO<sub>2</sub>

were performed. Unlike previous theoretical studies which mainly investigate the two end points of the process (*i.e.* TiO<sub>2</sub> and NaTiO<sub>2</sub>),<sup>22,43,46,53</sup> we theoretically calculate the crystalline structure changes of amorphous and anatase TiO<sub>2</sub> under step-by-step Na-ion uptake conditions. For sodiated amorphous TiO<sub>2</sub>-derived Na<sub>*x*</sub>TiO<sub>2</sub>, *x* is set in the sequence of 0.0555, 0.25, 0.5, 0.75, and 1 (Fig. S18†). For sodiated anatase TiO<sub>2</sub>-derived Na<sub>*x*</sub>TiO<sub>2</sub>, *x* is set in the sequence of 0.0625, 0.125, 0.25, 0.5, 0.75, and 1 (Fig. 6a–f). The Ti–O bond length distributions of sodiated anatase and amorphous TiO<sub>2</sub>-derived Na<sub>*x*</sub>TiO<sub>2</sub> are summarized and presented in Fig. 6g and h, respectively. The Na-ion insertion energy (*E*<sub>ins</sub>) is computed as:

$$E_{\text{ins}} = E_{\text{TiO}_2\text{:Na}} - E_{\text{TiO}_2} - E_{\text{Na}} \quad (3)$$

where *E*<sub>TiO<sub>2</sub>:Na</sub> is the total energy of the final system, *E*<sub>TiO<sub>2</sub></sub> is the energy of the host lattice in its equilibrium structure, and *E*<sub>Na</sub> is the energy of a single Na atom taken from the total energy of the bulk metallic Na. The cell parameters and *E*<sub>ins</sub> for the anatase and amorphous TiO<sub>2</sub>-derived Na<sub>*x*</sub>TiO<sub>2</sub> are presented in Table 1.

For amorphous TiO<sub>2</sub>, a 153-atom supercell of size about 11.53 × 11.53 × 9.87 Å<sup>3</sup> was used. The average coordination number of Ti (with a cutoff for the Ti–O bond of 2.5 Å) is 5.5 in the relaxed structure with an average Ti–O bond length of 1.99 Å, which are in good agreement with the measured experimental values for amorphous titania.<sup>74</sup> As demonstrated in Table 1 and Fig. 6h, sodiation (0 ≤ *x* ≤ 1) only has mild effects on the Ti–O bond length distribution. This indicates that the random arrangement of Ti and O atoms of amorphous titania provides plenty of insertion sites for Na-ion insertion.<sup>43,75</sup> The steadily increased but negative *E*<sub>ins</sub> further confirms the thermodynamically favorable conditions of amorphous TiO<sub>2</sub> for Na-ion insertion (Table 1).

For anatase TiO<sub>2</sub>, a 2 × 2 × 1 supercell (146 atoms, 7.64 × 7.64 × 9.7 Å<sup>3</sup>) was used for the calculation of sodiation. As shown in Fig. 6a–f, the theoretically crystalline Na<sub>*x*</sub>TiO<sub>2</sub> undergoes structure transformation along with Na-ion insertion (Fig. 6g). Similar to the previous results,<sup>22,43</sup> Na-ions can thermodynamically accommodate in the one-dimensional zigzag chains consisting of distorted edge-sharing octahedra (Fig. 6f). The length of Ti–O bonds of anatase-derived crystalline NaTiO<sub>2</sub> is in the range from 2.04 to 2.12 Å (top figure of Fig. 6g). Given that the Ti–O bond length of Ti<sub>2</sub>O<sub>3</sub> varies over the 2.03–2.07 Å range<sup>76</sup> and the Ti–O bond length of solid-phase reaction-prepared NaTiO<sub>2</sub> is *ca.* 2.09,<sup>77</sup> the simulated crystalline NaTiO<sub>2</sub> could be favorable because there is only a small crystal structure deformation.<sup>78</sup>

On the other hand, the analysis of the Ti–O bond length changes along with the step-by-step sodiation provides some new insights. During the initial sodiation (*x* = 0.0625), the inserted Na-ions demonstrate a fivefold-coordinated environment and locate in the anatase octahedral sites with a displacement of *ca.* 0.5 Å, giving rise to prolonged and compensatorily shortened Ti–O bond lengths of 2.08 Å and 1.95 Å along the *c* axis (Fig. 6a). The small changes of Ti–O bonds and the *E*<sub>ins</sub> of −0.89 eV indicate the thermodynamic stability of crystalline Na<sub>0.0625</sub>TiO<sub>2</sub>.<sup>75</sup> The sodiated anatase product of





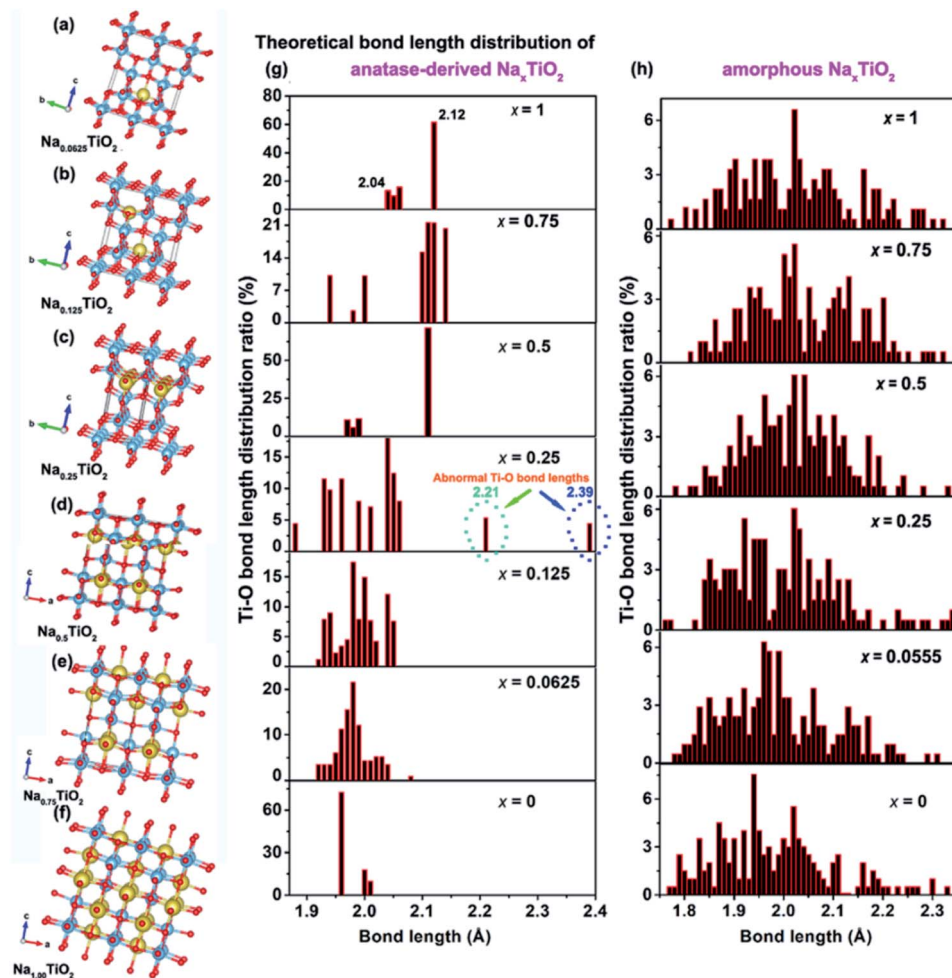


Fig. 6 Theoretical structures of anatase  $\text{TiO}_2$ -derived crystalline  $\text{Na}_{0.0625}\text{TiO}_2$  (a),  $\text{Na}_{0.125}\text{TiO}_2$  (b),  $\text{Na}_{0.25}\text{TiO}_2$  (c),  $\text{Na}_{0.5}\text{TiO}_2$  (d),  $\text{Na}_{0.75}\text{TiO}_2$  (e), and  $\text{NaTiO}_2$  (f). The Ti–O bond length distribution of anatase (g) and amorphous (h)  $\text{TiO}_2$ -derived  $\text{Na}_x\text{TiO}_2$  under different sodiation states.

$\text{Na}_{0.125}\text{TiO}_2$  is also theoretically stable as demonstrated from the Ti–O bond length distribution and  $E_{\text{ins}}$  (Fig. 6b). A significant difference occurs when  $x = 0.25$  (Fig. 6c). In crystalline  $\text{Na}_{0.25}\text{TiO}_2$ , because of the strong electron overlap repulsion and Coulomb repulsion among adjacent Na-ions as well as between

the Na-ions and Ti-ions,<sup>61,75</sup> the lengths of Ti–O bonds along the  $c$  axis are further increased to 2.21 and 2.39 Å with compensatory Ti–O bond lengths of 1.89 Å and 1.88 Å in the opposite direction along the  $c$  axis (Fig. 6c). The prolonged Ti–O lengths of 2.21 and 2.39 Å are much larger than those of  $\text{Ti}_2\text{O}_3$ ,

Table 1 Cell parameters for the anatase- and amorphous-derived theoretical  $\text{Na}_x\text{TiO}_2$  at different concentrations ( $x$ )

Samples	Insertion energy (eV)	$a$ (Å)	$b$ (Å)	$c$ (Å)	Volume (Å <sup>3</sup> )	Theoretical capacity (mA h g <sup>−1</sup> )
Anatase $\text{TiO}_2$	—	3.82	3.82	9.69	141.40	—
$\text{Na}_{0.0625}\text{TiO}_2$	−0.89	3.83	3.83	9.64	141.41	21
$\text{Na}_{0.125}\text{TiO}_2$	−0.79	3.90	3.90	9.49	144.34	42
$\text{Na}_{0.2500}\text{TiO}_2$	−0.77	4.05	3.80	9.68	148.98	84
$\text{Na}_{0.500}\text{TiO}_2$	−0.71	4.12	4.12	9.08	154.13	168
$\text{Na}_{0.7500}\text{TiO}_2$	−0.83	4.21	4.21	9.00	159.29	252
$\text{Na}_{1.000}\text{TiO}_2$	−0.87	4.32	4.32	8.88	166.47	336
Amorphous $\text{TiO}_2$	—	11.59	11.53	9.87	1317.85	—
$\text{Na}_{0.0555}\text{TiO}_2$	−1.12	11.49	11.63	9.76	1304.45	19
$\text{Na}_{0.2500}\text{TiO}_2$	−0.72	12.26	11.53	9.92	1400.32	84
$\text{Na}_{0.5000}\text{TiO}_2$	−0.50	12.55	12.91	9.07	1470.13	168
$\text{Na}_{0.7500}\text{TiO}_2$	−0.47	13.30	13.14	9.14	1597.18	252
$\text{Na}_{1.0000}\text{TiO}_2$	−0.37	13.44	13.22	9.31	1654.24	336



indicating that it is kinetically and thermodynamically unfavorable. Thus,  $\text{Na}_{0.25}\text{TiO}_2$  will disintegrate before  $\text{NaTiO}_2$  is obtained, although the crystalline  $\text{Na}_{0.5}\text{TiO}_2$  (Fig. 6d) and  $\text{Na}_{0.75}\text{TiO}_2$  (Fig. 6e) are theoretically stable. Furthermore, as demonstrated in the previous experimental and computational reports,<sup>5,10,17</sup> the Na-ion transport in anatase  $\text{TiO}_2$  is by “hopping” between two octahedral vacant sites. Increased Ti–O bond length could reasonably increase the Na-ion transport path length, kinetically hindering further sodiation in crystalline  $\text{Na}_{0.25}\text{TiO}_2$  to crystalline  $\text{Na}_{0.5}\text{TiO}_2$ . Such an increased Na-ion insertion barrier is reflected by the significantly increased  $E_{\text{ins}}$  between  $\text{Na}_{0.25}\text{TiO}_2$  (−0.77 eV) and  $\text{Na}_{0.5}\text{TiO}_2$  (−0.71 eV) (Table 1). Fig. S19† demonstrates the theoretical discharge curves of amorphous and anatase  $\text{TiO}_2$  along with the increase of discharge capacity up to  $336 \text{ mA h g}^{-1}$  based on the calculation data shown in Table 1. As shown in Fig. S19,† the amorphous  $\text{TiO}_2$  theoretically demonstrates a continuous voltage decrease along with the Na-ion uptake, which is consistent with the experimental GITT discharge curve of amorphous  $\text{TiO}_2$  shown in Fig. 3a and 4a. On the other hand, theoretically, the anatase  $\text{TiO}_2$  should take in Na-ions in a phase transformation manner with a small voltage vibration between 0.7 and 0.9 V (Fig. S19†). In contrast, the practical GITT discharge curve shows an unstable phase transformation and a following crystal structure disintegration before reaching  $\text{NaTiO}_2$  (Fig. 3b, c and 4b, c). Thus, it is further confirmed that the inevitable crystal structure disintegration occurs in practical measurements using a- $\text{TiO}_2$  as anodes for SIBs. Notably, as shown in Table 1, from a- $\text{TiO}_2$  to  $\text{Na}_{0.25}\text{TiO}_2$ , the Na-ion uptake into the octahedral sites gives rise to the expansion of the lattice in the *a*-axis from 11.59 to 12.26 Å, *i.e.*, theoretically small shifts of (200) and (101) crystalline plane XRD peaks to lower  $2\theta$  angles. Then crystal structure disintegration occurs upon further sodiation. These results are consistent with previously reported experimental phenomena about sodiation of high-crystallinity a- $\text{TiO}_2$  nanoparticles. During sodiation/desodiation, a- $\text{TiO}_2$  shows a small reversible shift of XRD peaks and a continuous decrease of XRD peak strength upon cycling.<sup>15,18,21,25,31,35,37,49</sup> These phenomena can be assigned to some of the a- $\text{TiO}_2$  particles that undergo reversible phase transition while the whole a- $\text{TiO}_2$  suffers continuous crystal structure disintegration during cycling measurements. Furthermore, research has also demonstrated that the crystal structure disintegration can more feasibly occur in doped a- $\text{TiO}_2$  (such as niobium-doped,<sup>79</sup> nickel-doped<sup>80</sup> and nickel/nitrogen-codoped  $\text{TiO}_2$  (ref. 81)), because their doped crystal structures are more susceptible to disintegration.

### 3.5 Proposed sodiation/de-sodiation mechanism in anatase $\text{TiO}_2$

According to the above thermodynamics and kinetics analysis, a sodiation/de-sodiation mechanism of a- $\text{TiO}_2$  is proposed. During the initial sodiation to 0.01 V, when the redox occurs under a near-equilibrium state, the sodium-ion uptake in a- $\text{TiO}_2$  sequentially includes three states: (1) sodium-ion insertion-derived irreversible phase transition; (2) then structural relaxation into amorphous and

low-crystallinity products; (3) further generation of metallic titanium and metallic sodium plating. In the following discharge/charge cycles, the amorphous and low-crystallinity products act as the main sodium storage hosts. Furthermore, the sodiation-derived compounds and electrochemical energy storage properties of a- $\text{TiO}_2$  can be tuned using the applied discharge/charge current density, potential windows and crystallinity when the sodiation is under non-equilibrium conditions. Notably, the a- $\text{TiO}_2$  materials with a relatively low crystallinity could demonstrate better rate performance because they can be more kinetically feasible to disintegration during the initial Na-ion uptake process. Furthermore, by doping a- $\text{TiO}_2$  with suitable elements which can alleviate the a- $\text{TiO}_2$  lattice integrity, the doped a- $\text{TiO}_2$  also can demonstrate high rate performance because of the facilitated crystal structure disintegration of the initial Na-ion uptake process.

### 3.6 Hybrid capacitors with anatase $\text{TiO}_2$ anodes

Based on the above results, it is found that the low crys- $\text{TiO}_2$  electrode delivers high capability after the electrochemical activation at  $15 \text{ mA g}^{-1}$ , indicating its suitability for organic hybrid capacitors.<sup>57,59</sup> The low crys- $\text{TiO}_2$  nanoparticles and commercial activated carbon (AC, BET specific surface area of  $2084.15 \text{ m}^2 \text{ g}^{-1}$ , XinSen Carbon Industry Co., Ltd) were, respectively, used as anode and cathode materials.

Fig. S20a† shows the typical CV curves of the AC electrode from 2 to 50  $\text{mV s}^{-1}$  between 2.5 and 4.0 V (vs.  $\text{Na/Na}^+$ ). The featureless shape indicates electrochemical double layer capacitance behavior.<sup>82</sup> The specific capacity of the AC electrode was determined with galvanostatic charge/discharge measurements (Fig. S20b, c†). Furthermore, the unchanged CV curves at 20  $\text{mV s}^{-1}$  for 100 cycles indicate its electrochemical stability (Fig. S20d†). For the assembly of hybrid capacitors, the optimum mass ratio of the anode and cathode is calculated using the specific capacity at  $50 \text{ mA g}^{-1}$  based on balancing the charge storages in the cathode and anode. The mass ratio of the low crys- $\text{TiO}_2$  and the AC is set as 1 : 5. Before the assembly of the capacitor, the low crys- $\text{TiO}_2$  electrode was run through one discharge/charge cycle and then fully sodiated in half-cells at  $15 \text{ mA g}^{-1}$ . The assembled hybrid capacitor was named the low crys- $\text{TiO}_2$ //AC. The capacity of the capacitor was determined by the mass of anodes.

The charge/discharge profiles and rate performance of the assembled low crys- $\text{TiO}_2$ //AC capacitors are, respectively, demonstrated in Fig. S21a and b.† The galvanostatic charge/discharge profiles of the low crys- $\text{TiO}_2$ //AC exhibit an almost triangular shape with small deviations from linearity, indicative of the capacitive energy storage nature of the low crys- $\text{TiO}_2$  (Fig. S21a†).<sup>82,83</sup> Due to the high Na-ion storage in a- $\text{TiO}_2$  anodes, the low crys- $\text{TiO}_2$ //AC hybrid capacitor demonstrates high capability performance over the potential window from 1 to 3 V. The hybrid capacitor delivers an energy density of  $18.9 \text{ W h kg}^{-1}$  in 11.3 min (Fig. S21b†). Notably, at  $2 \text{ A g}^{-1}$ , a short time of 5.3 s is needed to fulfil the discharge with a highly maintained energy density of  $5.79 \text{ W h kg}^{-1}$ . In addition, the assembled low crys- $\text{TiO}_2$ //AC capacitor shows impressive cycling stability. As shown in Fig. S21c,† after 2500 cycles at  $200 \text{ mA g}^{-1}$ , 70% of the initial capacity of the low crys- $\text{TiO}_2$ //AC



capacitor is retained, indicating the stable and reversible sodiation/de-sodiation kinetics in the low crys-TiO<sub>2</sub> anodes. As shown in Fig. S22a, b,† TEM examination shows that the low crys-TiO<sub>2</sub> nanoparticles maintain their morphology after 2500 cycles at 200 mA g<sup>-1</sup>. And the amorphous SAED pattern (Fig. S22c†) further confirms that there is a crystal structure disintegration process during the Na-ion uptake/release cycles.

## 4. Conclusions

In summary, the sodiation/de-sodiation thermodynamics and kinetics of a-TiO<sub>2</sub> are investigated by combining experimental analysis in near-equilibrium redox states and theoretical calculation of sodiated compounds under step-by-step Na-ion uptake conditions. It is found that the a-TiO<sub>2</sub> sequentially undergoes a phase transition and a following irreversible crystal structure disintegration during the initial Na-ion uptake process. Meanwhile, it is also found that the sodiation-derived compounds and the electrochemical energy storage properties are influenced by the applied discharge/charge current density, potential windows and crystallinity of a-TiO<sub>2</sub> particles when the Na-ion insertion is under non-equilibrium conditions. Notably, based on the experimental and theoretical calculation results, given that the crystal structure disintegration of a-TiO<sub>2</sub> is crystallinity-dependent, preparation of a-TiO<sub>2</sub> materials with low crystallinity and/or doping could be effective approaches to achieve high performance in a-TiO<sub>2</sub> anodes for sodium-ion batteries.

## Conflicts of interest

There are no conflicts to declare.

## Acknowledgements

This work was supported by the NSFC/RGC Joint Research Scheme 2020/21 (Project No: N\_CityU104/20) and the Science and Technology Foundation of Guizhou Province of China (No. qian ke he ji chu [2017] 1065).

## References

- 1 J. You, Y. Guo, R. Guo and X. Liu, *Chem. Eng. J.*, 2019, **373**, 624–641.
- 2 F. W. Low and C. W. Lai, *Renewable Sustainable Energy Rev.*, 2018, **82**, 103–125.
- 3 X. Lu, G. Wang, T. Zhai, M. Yu, J. Gan, Y. Tong and Y. Li, *Nano Lett.*, 2012, **12**, 1690–1696.
- 4 Z. Liu, A. Daali, G. g. Xu, M. Zhuang, X. Zuo, C. Sun, Y. Liu, Y. Cai, M. Hossain, H. Liu, K. Amine and Z. Luo, *Nano Lett.*, 2020, **20**, 3844–3851.
- 5 C. Chen, Y. Wen, X. Hu, X. Ji, M. Yan, L. Mai, P. Hu, B. Shan and Y. Huang, *Nat. Commun.*, 2015, **6**, 6929.
- 6 L. Cao, X. Gao, B. Zhang, X. Ou, J. Zhang and W. Luo, *ACS Nano*, 2020, **14**, 3610–3620.
- 7 Y. Kaneti, J. Zhang, Y. He, Z. Wang, S. Tanaka, Md. Hossain, Z. Pan, B. Xiang, Q. Yang and Y. Yamauchi, *J. Mater. Chem. A*, 2017, **5**, 15356–15366.
- 8 J. Wu a, J. Liu, J. Cui, S. Yao, M. Ihsan-Ul-Haq, N. Mubarak, E. Quattrocchi, F. Ciucci and J. Kim, *J. Mater. Chem. A*, 2020, **8**, 2114–2122.
- 9 N. Wang, C. Chu, X. Xu, Y. Du, J. Yang, Z. Bai and S. Dou, *Adv. Energy Mater.*, 2018, **8**, 1801888.
- 10 D. Lin, L. Lyu, K. Li, G. Chen, H. Yaoa, F. Kang, B. Li and L. Zhou, *J. Mater. Chem. A*, 2021, **9**, 9256–9265.
- 11 Z. Tong, S. Liu, X. Li, L. Mai, J. Zhao and Y. Li, *Nanoscale*, 2018, **10**, 3254–3261.
- 12 Y. Li, S. Wang, Y. He, L. Tang, Y. Kaneti, W. Lv, Z. Lin, B. Li, Q. Yang and F. Kang, *J. Mater. Chem. A*, 2017, **5**, 4359–4367.
- 13 K. Li, B. Li, J. Wu, F. Kang, J. Kim and T. Zhang, *ACS Appl. Mater. Interfaces*, 2017, **9**, 35917–35926.
- 14 J. Wu, M. Ihsan-Ul-Haq, F. Ciucci, B. Huang and J.-K. Kim, *Energy Storage Mater.*, 2021, **34**, 582–628.
- 15 K.-T. Kim, G. Ali, K. Y. Chung, C. S. Yoon, H. Yashiro, Y.-K. Sun, J. Lu, K. Amine and S.-T. Myung, *Nano Lett.*, 2014, **14**, 416–422.
- 16 L. Zhao, T. Tang, W. Chen, X. Feng and L. Mi, *Green Energy Environ.*, 2018, **3**, 277–285.
- 17 Z. Chen, L. Xu, Q. Chen, P. Hu, Z. Liu, Q. Yu, T. Zhu, H. Liu, G. Hu, Z. Zhu, L. Zhou and L. Mai, *J. Mater. Chem. A*, 2019, **7**, 6740–6746.
- 18 R. Luo, Y. Ma, W. Qu, J. Qian, L. Li, F. Wu and R. Chen, *ACS Appl. Mater. Interfaces*, 2020, **12**, 23939–23950.
- 19 W. Li, M. Fukunishi, B. J. Morgan, O. J. Borkiewicz, K. W. Chapman, A. Maignan, O. I. Lebedev, J. Ma, H. Groult, S. Komaba and D. Dambournet, *Chem. Mater.*, 2017, **29**, 1836–1844.
- 20 Q. Zhang, H. He, X. Huang, J. Yan, Y. Tang and H. Wang, *Chem. Eng. J.*, 2018, **332**, 57–65.
- 21 L. M. Wu, D. Bresser, D. Buchholz, G. A. Giffin, C. R. Castro, A. Ochel and S. Passerini, *Adv. Energy Mater.*, 2015, **5**, 1401142.
- 22 D. Su, S. Dou and G. Wang, *Chem. Mater.*, 2015, **27**, 6022–6029.
- 23 Z. Liu, W. Zhang, Z. Zhou, X. Liu, H. Zhang and M. Wei, *ACS Appl. Energy Mater.*, 2020, **3**, 3619–3627.
- 24 L. Ma, X. Gao, W. Zhang, H. Yuan, Y. Hu, G. Zhu, R. Chen, T. Chen, Z. Tie, J. Liu, T. Wu and Z. Jin, *Nano Energy*, 2018, **53**, 91–96.
- 25 Y. Fang, Y. Zhang, C. Miao, K. Zhu, Y. Chen, F. Du, J. Yin, K. Ye, K. Cheng, J. Yan, G. Wang and D. Cao, *Nano-Micro Lett.*, 2020, **12**, 128.
- 26 Y. Liu, J. Liu, D. Bin, M. Hou, A. G. Tamirat, Y. Wang and Y. Xia, *ACS Appl. Mater. Interfaces*, 2018, **10**, 14818–14826.
- 27 W. Wang, M. Wu, P. Han, Y. Liu, L. He, Q. Huang, J. Wang, W. Yan, L. Fu and Y. Wu, *ACS Appl. Mater. Interfaces*, 2019, **11**, 3061–3069.
- 28 Z. Hong, K. Zhou, Z. Huang and M. Wei, *Sci. Rep.*, 2015, **5**, 11960.
- 29 N. Louvain, A. Henry, L. Daenens, B. Boury, L. Stievano and L. Monconduit, *CrystEngComm*, 2016, **18**, 4431–4437.
- 30 D. Lin, K. Li, Q. Wang, L. Lyu, B. Li and L. Zhou, *J. Mater. Chem. A*, 2019, **7**, 19297–19304.
- 31 K. Li, J. Zhang, D. Lin, D. Wang, B. Li, W. Lv, S. Sun, Y. He, F. Kang, Q. Yang, L. Zhou and T. Zhang, *Nat. Commun.*, 2019, **10**, 725.





- 32 L. Ling, Y. Bai, Y. Li, Q. Ni, Z. Wang, F. Wu and C. Wu, *ACS Appl. Mater. Interfaces*, 2017, **9**, 39432–39440.
- 33 W. Song, H. Zhao, J. Ye, M. Kang, S. Miao and Z. Li, *ACS Appl. Mater. Interfaces*, 2019, **11**, 17416–17424.
- 34 C. Ding, T. Nohira and R. Hagiwara, *Phys. Chem. Chem. Phys.*, 2016, **18**, 30770–30776.
- 35 J. Li, J. Liu, Q. Sun, M. N. Banis, X. Sun and T. Sham, *J. Phys. Chem. C*, 2017, **121**, 11773–11782.
- 36 Y. Liu, F. Zhao, J. Li, Y. Li, J. A. McLeod and L. Liu, *J. Mater. Chem. A*, 2017, **5**, 20005–20013.
- 37 G. Santoro, J. M. Amarilla, P. Tartaj and M. B. Vázquez-Santos, *Mater. Today Energy*, 2018, **10**, 23–27.
- 38 C. Deng, C. Ma, M. L. Lau, P. Skinner, Y. Liu, W. Xu, H. Zhou, Y. Ren, Y. Yin, B. Williford, M. Dahl and H. Xiong, *Electrochim. Acta*, 2019, **321**, 134723.
- 39 Z. Le, F. Liu, P. Nie, X. Li, X. Liu, Z. Bian, G. Chen, H. Wu and Y. Lu, *ACS Nano*, 2017, **11**, 2952–2960.
- 40 M. Fehse, A. Henry, A. Zitolo, B. Boury, N. Louvain and L. Stievano, *Appl. Sci.*, 2020, **10**, 5547.
- 41 G. Greco, K. A. Mazzio, X. Dou, E. Gericke, R. Wendt, M. Krumrey and S. Passerini, *ACS Appl. Energy Mater.*, 2019, **2**, 7142–7151.
- 42 H. He, Q. Gan, H. Wang, G. Xu, X. Zhang, D. Huang, F. Fu, Y. Tang, K. Amine and M. Shao, *Nano Energy*, 2018, **44**, 217–227.
- 43 M. Zhou, Y. Xu, J. Xiang, C. Wang, L. Liang, L. Wen, Y. Fang, Y. Mi and Y. Lei, *Adv. Energy Mater.*, 2016, **6**, 1600448.
- 44 H. He, Q. Zhang, H. Wang, H. Zhang, J. Li, Z. Peng, Y. Tang and M. Shao, *J. Power Sources*, 2017, **354**, 179–188.
- 45 H. He, D. Huang, W. Pang, D. Sun, Q. Wang, Y. Tang, X. Ji, Z. Guo and H. Wang, *Adv. Mater.*, 2018, **30**, 1801013.
- 46 J. Chen, B. Luo, Q. Chen, F. Li, Y. Guo, T. Wu, P. Peng, X. Qin, G. Wu, M. Cui, L. Liu, L. Chu, B. Jiang, Y. Li, X. Gong, Y. Chai, Y. Yang, Y. Chen, W. Huang, X. Liu and M. Li, *Adv. Mater.*, 2020, **32**, 1905578.
- 47 N. Lee, J. Jung, J. Lee, H. Jang, I. Kim and W. Ryu, *Electrochim. Acta*, 2018, **263**, 417–425.
- 48 W. Wei, M. Valvo, K. Edström and L. Nyholm, *ChemElectroChem*, 2018, **5**, 674–684.
- 49 J. Wang, J. Li, X. He, X. Zhang, B. Yan, X. Hou, L. Du, T. Placke, M. Winter and J. Li, *J. Power Sources*, 2020, **461**, 228129.
- 50 Z. Xu, K. Lim, K. Park, G. Yoon, W. Seong and K. Kang, *Adv. Funct. Mater.*, 2018, **28**, 1802099.
- 51 T. Gao, X. Ji, S. Hou, X. Fan, X. Li, C. Yang, F. Han, F. Wang, J. Jiang, K. Xu and C. Wang, *Adv. Mater.*, 2018, **30**, 1704313.
- 52 A. Ven, Z. Deng, S. Banerjee and S. Ong, *Chem. Rev.*, 2020, **120**, 6977–7019.
- 53 A. Massaro, A. Muñoz-García, P. Maddalena, F. Bella, G. Meligrana, C. Gerbaldi and M. Pavone, *Nanoscale Adv.*, 2020, **2**, 2745–2751.
- 54 Y. Zhu, Y. Xu, Y. Liu, C. Luo and C. Wang, *Nanoscale*, 2013, **5**, 780–787.
- 55 M. Wahid, D. Puthusseri, Y. Gawli, N. Sharma and S. Ogale, *ChemSusChem*, 2018, **11**, 506–526.
- 56 M. Liu, P. Zhang, Z. Qu, Y. Yan, C. Lai, T. Liu and S. Zhang, *Nat. Commun.*, 2019, **10**, 3917.
- 57 Z. Tong, S. Liu, Y. Zhou, J. Zhao, Y. Wu, Y. Wang and Y. Li, *Energy Storage Mater.*, 2018, **13**, 223–232.
- 58 Y. Cao, T. Zhang, X. Zhong, T. Zhai and H. Li, *Chem. Commun.*, 2019, **55**, 14761–14764.
- 59 V. Augustyn, P. Simon and B. Dunn, *Energy Environ. Sci.*, 2014, **7**, 1597–1614.
- 60 Y. Huang, C. Zhu, S. Zhang, X. Hu, K. Zhang, W. Zhou, S. Guo, F. Xu and H. Zeng, *Nano Lett.*, 2019, **19**, 1118–1123.
- 61 F. Bella, A. B. Muñoz-García, G. Meligrana, A. Lamberti, M. Destro, M. Pavone and C. Gerbaldi, *Nano Res.*, 2017, **10**, 2891–2903.
- 62 S. Gu, H. Wang, C. Wu, Y. Bai, H. Li and F. Wu, *Energy Storage Mater.*, 2017, **6**, 9–17.
- 63 Z. Tong, J. Hao, K. Zhang, J. Zhao, B. Su and Y. Li, *J. Mater. Chem. C*, 2014, **2**, 3651–3658.
- 64 Z. Tong, H. Xu, G. Liu, J. Zhao and Y. Li, *Electrochem. Commun.*, 2016, **69**, 46–49.
- 65 C. Deng, M. Lau, H. Barkholtz, H. Xu, R. Parrish, M. Xu, T. Xu, Y. Liu, H. Wang, J. Connell, K. Smith and H. Xiong, *Nanoscale*, 2017, **9**, 10757–10763.
- 66 Z. Li, F. Du, X. Bie, D. Zhang, Y. Cai, X. Cui, C. Wang, G. Chen and Y. Wei, *J. Phys. Chem. C*, 2010, **114**, 22751–22757.
- 67 M. Levi, K. Gamolsky, D. Aurbach, U. Heider and R. Oesten, *J. Electroanal. Chem.*, 1999, **477**, 32–40.
- 68 X. Wang, X. Yu, H. Li, X. Yang, J. McBreen and X. Huang, *Electrochem. Commun.*, 2008, **10**, 1347–1350.
- 69 Z. Cui, X. Guo and H. Li, *Energy Environ. Sci.*, 2015, **8**, 182–187.
- 70 K. Tang, X. Yu, J. Sun, H. Li and X. Huang, *Electrochim. Acta*, 2011, **56**, 4869–4875.
- 71 E. Allcorn, S. Kim and A. Manthiram, *Phys. Chem. Chem. Phys.*, 2015, **17**, 28837–28843.
- 72 Z. Tong, R. Yang, S. Wu, D. Shen, T. Jiao, K. Zhang, W. Zhang and C. S. Lee, *Small*, 2019, **15**, 1901272.
- 73 Z. Tong, R. Yang, S. Wu, D. Shen, T. Jiao, K. Zhang, W. Zhang and C.-S. Lee, *J. Mater. Chem. A*, 2019, **7**, 19581–19588.
- 74 V. Petkov, G. Holzhüter, U. Tröge, T. Gerber and B. Himme, *J. Non-Cryst. Solids*, 1998, **231**, 17–30.
- 75 F. Legrain, O. Malvi and S. Manzhos, *J. Power Sources*, 2015, **278**, 197–202.
- 76 L. F. Mattheiss, *J. Phys.: Condens. Matter*, 1996, **8**, 5987–5995.
- 77 D. Wu, X. Li, B. Xu, N. Twu, L. Liu and G. Ceder, *Energy Environ. Sci.*, 2015, **8**, 195–202.
- 78 R. P. Kolli and A. Devaraj, *Metals*, 2018, **8**, 506.
- 79 F. Zhao, B. Wang, Y. Tang, H. Ge, Z. Huang and H. Liu, *J. Mater. Chem. A*, 2015, **3**, 22969–22974.
- 80 D. Yan, C. Yu, D. Li, X. Zhang, J. Li, T. Lu and L. Pan, *J. Mater. Chem. A*, 2016, **4**, 11077–11085.
- 81 D. Yan, C. Yu, X. Zhang, J. Li, J. Li, T. Lu and L. Pan, *Electrochim. Acta*, 2017, **254**, 130–139.
- 82 Z. Tong, Y. Yang, J. Wang, J. Zhao, B. Su and Y. Li, *J. Mater. Chem. A*, 2014, **2**, 4642–4651.
- 83 S. Zhou, S. Wang, S. Zhou, H. Xu, J. Zhao, J. Wang and Y. Li, *Nanoscale*, 2020, **12**, 8934–8941.

